Wavelength-Dependent Wavefront Produced and Controlled in Optical Parametric Chirped-Pulse Amplification

Yirui Wang ⓘD, Wenhao Wang ⓘD, Yudong Tao, Jing Wang ⓘD, Jingui Ma ⓘD, Peng Yuan ⓘD, and Liejia Qian ⓘD

Abstract—**It is generally impossible to maintain tight focusing over a long distance because of diffraction; this so-called Rayleigh's curse may be broken for a femtosecond laser if the wavefront curvature varies with laser wavelength. This paper reports on a nonlinear technique to produce a wavelength-dependent wavefront. We reveal a wavelength-dependent wavefront mechanism that is induced in optical parametric chirped-pulse amplification (OPCPA) where the crystal effect of group-velocity mismatch (GVM) dominates. Both analytical and numerical investigations show that the sign of the produced wavefront can be changed by GVM, and the magnitude can be enhanced by multistage OPCPA. The results suggest that the Rayleigh range at a fixed beam waist size can be significantly increased by the OPCPA-induced wavelength-dependent wavefront.**

Index Terms—**Optical parametric amplifiers, rayleigh range, spatiotemporal couplings.**

I. INTRODUCTION

OPTICAL superresolution and a long Rayleigh range of tight focusing have long been desired in optics [1]–[4]. However, these desired characteristics are fundamentally limited by the nature of light diffraction [5]. On the one hand, the resolution of an optical imaging system, such as a camera, telescope, or microscope, is limited by the minimum separation between two incoherent point sources [6]. Such a resolution limitation, also termed Rayleigh's curse or criterion, greatly hinders the ability to identify finer details [7]. Recently, M. Paúr *et al.* demonstrated that Rayleigh's curse can be overcome with point spread function shaping [8]. The resolution achieved by the optimized measurement was nearly 16 times lower than that achieved by direct imaging. On the other hand, for an optical focusing system, the Rayleigh range is proportional to the square of the focal spot size, and one cannot simultaneously achieve a long Rayleigh range and small focal spot, which limits

applications such as laser processing [9], [10]. Nevertheless, ultrashort lasers with a broad spectrum show potential to break the limit of the Rayleigh range.

Pioneering work by F. Quéré [11] suggested the possibility of increasing the Rayleigh range through the use of the spatiotemporal coupling effects of ultrashort pulses. A wavelength-dependent wavefront (WWF) deliberately induced by a chromatic lens makes each frequency component focus at its own longitudinal position. Consequently, the overall Rayleigh range for all frequency components can be greatly extended around the focal plane. When the spectral bandwidth of a laser pulse is much less than the angular frequency of the laser beam, the effect of longitudinal chromatism is observed around the focal plane; i.e., the best focus position manifests as a linear function of the laser frequency. In addition, this approach may also be applicable for multiwavelength laser sources, such as those generated by long-period fiber gratings [12], [13]. D. H. Froula *et al.* [14] extended this approach by replacing a common chromatic lens with a Fresnel lens, resulting in an approximately 100 times increase in the Rayleigh range. However, such a WWF is determined by the glass dispersion of the lens, so that cannot be adjusted under a fixed wavelength. In this paper, we reveal that the WWF can be nonlinearly induced by spatiotemporal couplings in optical parametric chirped-pulse amplification (OPCPA), whose magnitude and sign can be easily adjusted.

Broadband OPCPA under an imperfect phase-matching condition can induce a nonlinear phase due to cascaded nonlinearity [15]. In particular, for an OPCPA that operates under group-velocity mismatch (GVM) and a Gaussian pump beam, such a nonlinear phase imposed on the signal is characterized by a linear dependence on laser frequency, and simultaneously a dependence on space [16]. The induced nonlinear spectral phase has been reported to be a spatiotemporal distortion that is detrimental to the OPCPA system [17]–[20]. From the view of space, such a space-dependent spectral phase manifests as the WWF, which is the research topic of this paper. This WWF in the spatial-spectral domain acts as a pulse-front curvature (PFC) in spatial-temporal domain by taking the Fourier transformation. It is intuitive to characterize the WWF magnitude by the strength of PFC. Fig. 1 illustrates the PFC of the signal after being amplified by a single-stage collinear OPCPA. When the idler travels faster than the signal (i.e., $\text{GVM}_{si} = 1/v_{gs} - 1/v_{gi} > 0$,
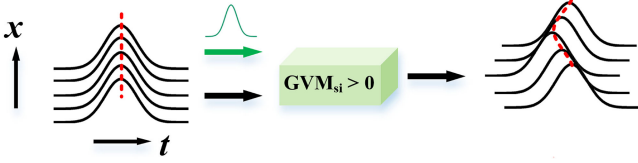
Fig. 1. Spatiotemporal illustration of the signal PFC induced in OPCPA with a positive GVM_{si}. The involved idler beam is not shown, assuming the dispersion of the stretcher and crystal acquired by the amplified signal is completely compensated by the pulse compressor.

where v_{gs}, v_{gi} denote the group-velocity of the signal and idler pulse, respectively), the signal experiences a positive value of Kerr-like cascaded nonlinearity, which reduces the signal velocity. By considering the Gaussian beam profiles of both the seed signal and pump, the signal beam center suffers from the largest cascaded nonlinearity and hence the largest velocity reduction, which results in a positive PFC, as shown in Fig. 1. Notably, a negative PFC can be produced if $GVM_{si} < 0$.

II. THEORETICAL ANALYSIS

The WWF produced with collinear OPCPA is the consequence of the space-dependent first-order spectral phase of cascaded nonlinearity. By solving the imaginary parts of the nonlinear coupled-wave equations in the small-signal amplification regime (i.e., pump nondepletion), the nonlinear spectral phase over the amplified signal spectrum is found to have a simplified form of [21]

$$\varphi_s = \varphi_{s0} - \Delta k L/2 + \arctan\left[\Delta k/(2g)\right], \quad (1)$$

where φ_{s0} is the initial phase of the signal, L is the crystal length, $\Delta k = k_p - k_s - k_i$ is the phase mismatch among the interacting waves (k_p, k_s, and k_i denote the wave vectors for the pump, signal and idler waves, respectively), and g is the small-signal gain coefficient. For a Gaussian-profile pump beam described by $I_p = I_{p0}\exp(-x^2/W_0^2)$, where I_{p0}, x and W_0 denote the peak intensity, transverse coordinate and $1/e$ radius of the beam waist, respectively, the small-signal gain coefficient is space dependent, as given by [22]

$$g(x) = \gamma e^{-x^2/2W_0^2}, \text{with } \gamma$$
$$= 4\pi d_{eff}[I_{p0}/(2\varepsilon_0 n_p n_s n_i c\lambda_s\lambda_i)]^{1/2}, \quad (2)$$

where d_{eff} denotes the effective nonlinear coefficient, n and λ are the refractive index and wavelength, respectively, with appropriate subscripts for the pump (p), signal (s), and idler (i).

In an OPCPA, the presence of GVM between the broadband signal and idler waves, i.e., $GVM_{si} \neq 0$, results in a frequency-dependent phase mismatch as given by:

$$\Delta k(\omega) = \Delta k_0 + GVM_{si}\Delta\omega, \quad (3)$$

where Δk_0 is the wave-vector mismatch at the signal central frequency ω_0 and $\Delta\omega = \omega - \omega_0$ is the frequency offset with respect to ω_0. Generally, the value of Δk_0 is set to zero. Substituting (2) and (3) into (1) yields:

$$\varphi_s = -GVM_{si}\Delta\omega L/2 + \arctan\left\{GVM_{si}\Delta\omega/[2g(x)]\right\}. \quad (4)$$

The first order approximation of (4) yields:

$$\varphi_s = \{-GVM_{si}L/2 + GVM_{si}/[2g(x)]\}\,\Delta\omega. \quad (5)$$

In addition to a constant term, the nonlinear phase has a term depending on x. It can be deduced from (5) that the spectral phase varies with x at a fixed frequency. By expanding (5) with respect to x, we have

$$\varphi_s(x) \approx \alpha_0 + \alpha\Delta\omega x^2, \text{ with } \alpha = GVM_{si}/(4\gamma W_0^2), \quad (6)$$

where α_0 is a space-independent phase and where the second term indicates the WWF, which is proportional to the GVM_{si} condition of OPCPA. Such a WWF can be characterized by the frequency-dependent wavefront curvature $R(\Delta\omega)$ as

$$1/R(\Delta\omega) = 2\alpha\Delta\omega/k_s. \quad (7)$$

On the one hand, this frequency-dependent wavefront curvature causes different frequency components to be focused at different longitudinal positions. By performing an inverse Fourier transform, one can obtain the PFC in space and time as

$$E(x,t) = A_0\left(x, t - \alpha_0 - \alpha x^2\right)\exp(i\omega_0 t), \quad (8)$$

where A_0 is the complex envelope. The strength of the induced PFC can be characterized by the α coefficient.

Numerical simulations were performed in three dimensions (x, t, and z), with variables of transverse position x, time t and propagation distance z. The seed signal had a full width at half maximum (FWHM) of 27 nm (80 THz) centered at 800 nm and a chirped-pulse FWHM duration of 600 fs. The pump laser adopted 1 ps, 515 nm, monochromatic pulses. The intensities of the pump and seed were 5 GW/cm^2 and 0.5 MW/cm^2, respectively, to ensure small-signal amplification. Both the pump and seed had Gaussian-shaped profiles in space and time with an equal beam waist of $W_0 = 2$ mm ($1/e$ radius). In practice, such a pump laser can be achieved by second-harmonic generation of a picosecond Yb:YAG thin-disk laser, while the broadband seed pulse is the output of a femtosecond Ti:sapphire regenerative amplifier system.

The fact that the nonlinear WWF [Eq. (6)] and PFC [Eq. (8)] produced by OPCPA are both governed by GVM_{si} implies that they can be canceled by adopting two OPCPA stages with opposite GVM_{si}. This scheme is important for some OPCPA applications wherein WWF and PFC exist as destructive distortions of the amplified signal, causing unacceptable degradation in the focused peak intensity [21]. Fig. 2(a) shows the schematic layout of such a two-stage OPCPA configuration. We designed the crystals used in two OPCPA stages: a 2-mm-thick Type-I β-BBO ($\theta = 22.7°$, $\varphi = 0°$) with a positive $GVM_{si} = 45$ fs/mm and a 1-mm-thick Type-II β-BBO ($\theta = 39.6°$, $\varphi = 30°$) with a negative $GVM_{si} = -129$ fs/mm. These two OPCPA stages successively imprinted opposite nonlinear spectral phases on the amplified signal pulse and thus canceled each other. Both OPCPA stages operated in the collinear phase-matching geometry and the small-signal amplification regime.

The spatiotemporal profile of the compressed signal [Fig. 2(b)] output from the first OPCPA stage explicitly shows the presence of PFC, as highlighted by the white dashed curve. The spectral phase of this signal pulse was also space dependent.
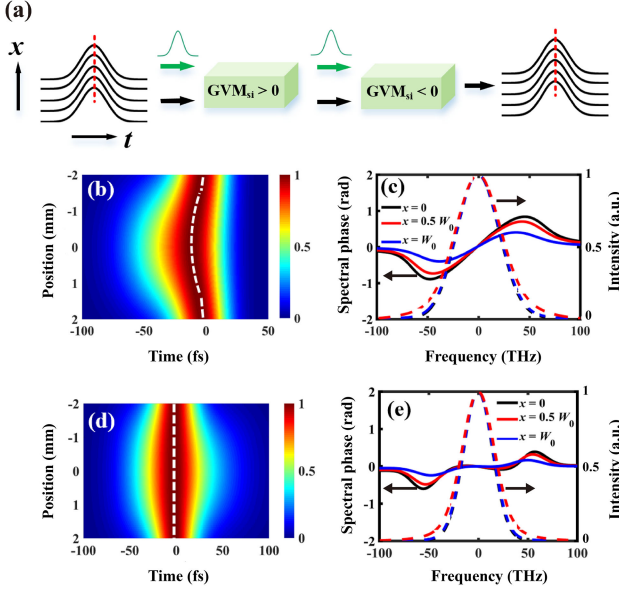
Fig. 2. Impact of the GVM_{si} sign on the OPCPA-induced PFC. (a) Schematic of two-stage OPCPA with opposite GVM_{si} signs. (b) Spatiotemporal intensity profile of the compressed signal. (c) Signal spectra and the nonlinear spectral phase sampled at three different spatial positions ($x = 0$, $0.5 W_0$ and W_0) calculated for the first OPCPA stage, (d) and (e) Calculated for the second OPCPA stage.

As shown in Fig. 2(c), the nonlinear spectral phase exhibited mainly a first-order characteristic (i.e., linear within the spectrum), but with different slopes at different x positions. The spectra at the beam center ($x = 0$) and beam edge ($x = W_0$) show a good overlap, which indicates that the nonlinear phase induced only the WWF and had little effect on other spatiotemporal properties, such as the pulse duration and the second-order dispersion.

The output chirped signal of the first stage was then injected into the second OPCPA stage with a negative GVM_{si}. As expected, the PFC near the beam center vanished after the second OPCPA, and a nearly ideal pulse front was obtained [Fig. 2(d)]. That is, the pulses within the whole beam simultaneously reached their peak intensity. The final output spectral phase was nearly flat for most frequency components from –40 to 40 THz [Fig. 2(e)]. These results confirm that the PFC produced by OPCPA can be controlled by changing the GVM_{si} environment through a multistage configuration.

Next, we characterize the WWF induced by OPCPA. Fig. 3 shows the calculated WWF produced by the first OPCPA with $GVM_{si} > 0$. The central frequency component ($\Delta\omega = 0$) maintained a plane wave (black line) owing to perfect phase matching ($\Delta k = 0$). Other frequency components were approximately spherical waves with varied curvatures, as has been predicted in (7). In particular, those waves of higher frequencies were convergent and hence focused before the lens focal plane, and the lower-frequency components were divergent and hence focused behind the lens focal plane. As a result, the overall Rayleigh range for all frequency components could be much larger than that of a conventional laser beam without WWF. In other words,
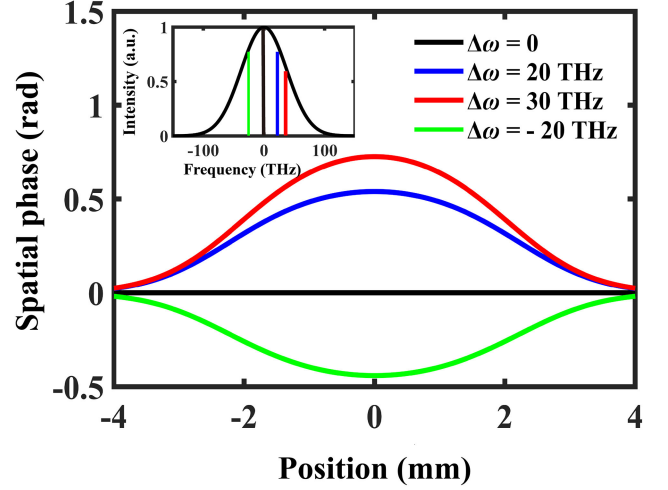

Fig. 3. Calculated wavefronts at four frequencies of $\Delta\omega = 0$, 20, 30 and -20 THz. The inset shows the seed signal spectrum with those four frequencies in the calculation.
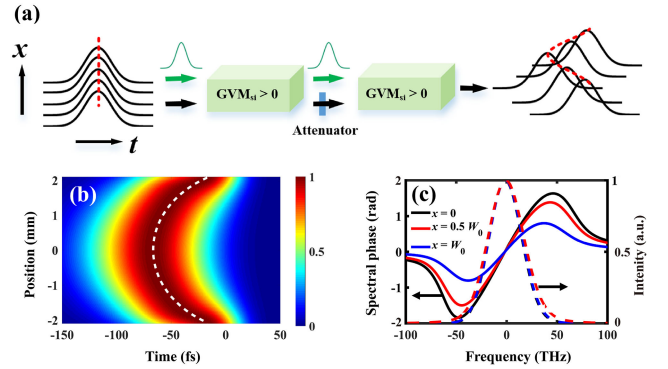

Fig. 4. (a) Tandem configuration consisting of two OPCPAs with positive GVM_{si}. The signal propagates through the two OPCPA stages successively with an intermediate attenuator. (b) Spatiotemporal intensity profile of the output signal after pulse compression. (c) Signal spectra (dashed lines) and the nonlinear spectral phase (solid lines) sampled at $x = 0$, $0.5 W_0$ and W_0 for the output signal.

the induced WWF increases the Rayleigh range that is limited by light diffraction.

III. ENHANCEMENT OF WWF AND RAYLEIGH RANGE

A further enhancement of the WWF is desired for obtaining a larger Rayleigh range. To achieve this, we propose a tandem configuration consisting of multistage OPCPAs with the same GVM_{si} signs. Taking a two-stage configuration as shown in Fig. 4(a) for example, the simulation parameters were set the same as those for Fig. 2, except that the second OPCPA stage here adopted a Type-I BBO crystal with positive GVM_{si} instead of a Type-II BBO crystal. Additionally, a signal attenuator was used to reduce the signal energy, which ensured that both OPCPA stages operated in the small-signal amplification regime. Fig. 4(b) depicts the PFC of the amplified signal beam. The temporal delay between the pulse front at the beam center and that at the beam edge increased to 30 fs, which was significantly larger than that ($\sim$15 fs) induced by the single-stage OPCPA,
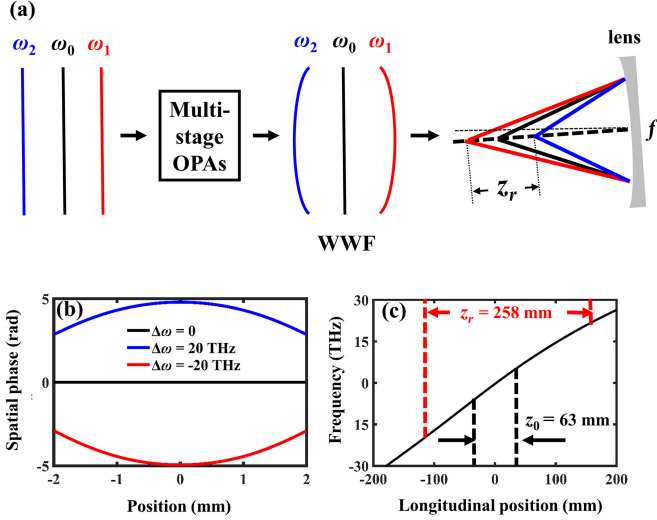
(a)

WWF

Fig. 6. (a) Calculated WWF for the signal beam output from 9-stage OPCPA, wherein $\text{GVM}_{si} < 0$ in all stages of OPCPA. The wavefronts at the three frequency components of ω_0 (central frequency), ω_1 ($= \omega_0 - 20$ THz) and ω_2 ($= \omega_0 + 20$ THz) are plotted as representatives. (b) Best focusing position for each frequency component within the signal spectrum.

Fig. 5. (a) Schematic of the longitudinal chromatism caused by focusing the signal beam with a WWF. (b) Calculated WWF for the signal beam output from 9-stage OPCPA, wherein $\text{GVM}_{si} > 0$ in all stages of OPCPA. The wavefronts at the three frequency components of ω_0 (central frequency), ω_1 ($= \omega_0 - 20$ THz) and ω_2 ($= \omega_0 + 20$ THz) are plotted as representatives. (c) Best focusing position for each frequency component within the signal spectrum, where $z = 0$ represents the best focusing position of the central frequency component.

as shown in Fig. 2(b). Correspondingly, the nonlinear spectral phase increased and still maintained a first-order characteristic [Fig. 4(c)].

Note that the WWF magnitude of each stage does not depend on the seed intensity and remains unchanged in the small-signal amplification regime. Therefore, by adopting a tandem configuration of *N*-stage OPCPA, the enhanced WWF characterized by the wavelength-dependent radius of wavefront curvature can be evaluated by:

$$\Lambda \approx N/R(\Delta\omega) = 2N\alpha\Delta\omega/k_s. \quad (9)$$

Because of the overall temporal delay of the amplified signal, as shown in (6), synchronization between the signal and pump is necessary for all stages unless the pump pulse duration is large enough.

When the signal beam with the WWF was focused by a lens without chromatic aberration (e.g., a concave mirror), each frequency component exhibited the best focus at different longitudinal position z, as illustrated by Fig. 5(a). That is, the far-field exhibited longitudinal chromatism. We next simulated the longitudinal chromatism for the output signal from a 9-stage OPCPA tandem. All the OPCPA stages adopted the same pump and crystal parameters as those in Fig. 4. The attenuation rate between the two stages was set to 70%. The output signal beam exhibited a PFC of $\alpha = 2.2$ fs/cm^2 in the near field. Fig. 5(b) depicts the corresponding WWF, indicating that the red frequency component acquired a divergent wavefront, while the blue frequency component acquired a convergent wavefront. As a result, the best focus positions linearly varied with the signal frequency, as plotted in Fig. 5(c). This longitudinal chromatism then led to an extended frequency-integrated Rayleigh length z_r. By using a concave mirror of 1 m focal length
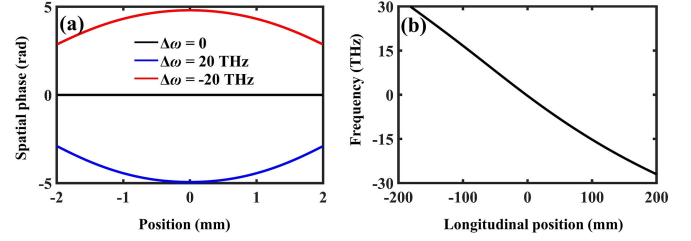
in simulations, the Rayleigh distance z_0 of the signal beam at the central frequency was calculated as 63 mm, while the frequency-integrated Rayleigh length was enlarged to 258 mm. The exceptionally large depth of focus presents an opportunity to extend interaction lengths and overcome current limitations in coherent imaging [23], photon accelerators [24], laser-plasma amplifiers [25], laser-wakefield accelerators [26], high-order frequency conversion [27] and photon-electron light sources [28]. In addition, a further increase in z_r can be achieved by optimizing the GVM_{si} and the stages of OPCPA in tandem. These results can be extended to a general situation. Assuming an ideal lens with a focal length f, the imaging equation can be given by $1/R'(\Delta\omega) + 1/R(\Delta\omega) = 1/f$, where $R'(\Delta\omega)$ is the frequency-dependent wavefront curvature after the lens. Therefore, the increased Rayleigh range by the WWF can be described as follows [11]:

$$z_r = R'(\Delta\omega) = 2f^2\alpha\Delta\omega/k_{s0}. \quad (10)$$

Specifically, we obtain $z_r = f^2\Lambda$ for *N*-stage OPCPA tandem. According to the definition of the conventional Rayleigh distance $z_0 = 2f^2/(k_{s0}W_0^2)$, the enhancement factor of the Rayleigh range due to the WWF is thus obtained:

$$M = z_r/z_0 = \text{GVM}_{si}\Delta\omega/(4\gamma) \propto (\gamma L)^{-1/2}. \quad (11)$$

According to (11), the increment of the Rayleigh range due to the WWF can be controlled by the nonlinear coupling coefficient γ and the crystal length L.

The WWF originating from cascaded nonlinearity is determined by the sign and magnitude of the GVM_{si} in OPCPA. This implies that the longitudinal chromatism resulting from WWF can be flexibly controlled in both sign and magnitude. To demonstrate this, we finally simulated a 9-stage OPCPA tandem of the same simulation parameters as those used in Fig. 5, except for adopting negative GVM_{si} instead of positive GVM_{si} for each OPCPA stage. The amplified signal exhibited a WWF [Fig. 6(a)] opposite to that depicted in Fig. 5(b), for which the blue (red) frequency component acquired a divergent (convergent) wavefront. After focusing with an ideal lens, the best focus of the higher-frequency component was located farther from that of the lower-frequency component, as illustrated in Fig. 6(b). These results indicated that by simply changing the sign of GVM_{si}, longitudinal chromatism with an opposite sign can be obtained.

In addition, the magnitude of longitudinal chromatism can also be increased with GVM$_{si}$ and/or OPCPA stages. In contrast, it is difficult to change the sign of longitudinal chromatism in the linear optical approach using a lens [11], [14]. The production of such controllable longitudinal chromatism might provide a novel approach to the design of achromatic optical systems.

IV. Conclusion

In conclusion, we have demonstrated that a WWF can be produced and controlled in OPCPA. For a monochromatic component of a broadband laser, the wavefront variation does not affect the nature of light diffraction. However, for the overall frequency components of a broadband ultrashort laser, the WWF equivalently changes the behavior of light diffraction. Thus, Rayleigh's curse can be overcome through the WWF, resulting in a larger Rayleigh range for a fixed beam waist size. Full numerical simulations show that the magnitude of the WWF can be enhanced by implementing multi-stages of OPCPA in tandem, and the resultant WWF can be evaluated by (9). The WWF causes a wavelength-dependent radius of wavefront curvature and affects beam focusing. The feasibility of applying the enhanced WWF to manipulate the longitudinal chromatic is also verified, gaining four times the Rayleigh range. A generalized conclusion on the WWF-enhanced Rayleigh range is given, showing that the Rayleigh range can be controlled by an appropriate design of multistage OPCPA. By reversing the sign of GVM$_{si}$, the chromatism that is unattainable by lenses is achieved, i.e., the red frequency components experience a converging wavefront, while the blue components experience a divergent wavefront. The results presented in this work may solve the problem that a WWF can be induced only by normal dispersion in a lens, indicating that the WWF produced in OPCPA can be manipulated in a more flexible manner.

References

[1] T. Dertinger, R. Colyer, R. Vogel, J. Enderlein, and S. Weiss, "Achieving increased resolution and more pixels with superresolution optical fluctuation imaging (SOFI)," *Opt. Exp.*, vol. 18, no. 18, pp. 18875–18885, Aug. 2010, doi: 10.1364/OE.18.018875.

[2] J. B. Stewart, B. E. A. Saleh, M. C. Teich, and J. T. Fourkas, "Experimental demonstration of polarization-assisted transverse and axial optical super-resolution," *Opt. Commun.*, vol. 241, no. 4–6, pp. 315–319, Nov. 2004, doi: 10.1016/j.optcom.2004.07.042.

[3] J. Liu, J. Lin, H. Zhao, and S. Liu, "Analysis of closed-boundary cylindrical microlenses with long focal depth designed by the general focal length function," *Opt. Commun.*, vol. 281, no. 17, pp. 4188–4193, Sep. 2008, doi: 10.1016/j.optcom.2008.04.067.

[4] W. Zhao, Z. Li, L. Qiu, H. Ren, and R. Shao, "Large-aperture laser differential confocal ultra-long focal length measurement and its system," *Opt. Exp.*, vol. 23, no. 13, pp. 17379–17393, Jun. 2015, doi: 10.1364/OE.23.017379.

[5] Y. Dan, S. Zeng, B. Hao, and B. Zhang, "Range of turbulence-independent propagation and Rayleigh range of partially coherent beams in atmospheric turbulence," *J. Opt. Soc. Amer. A*, vol. 27, no. 3, pp. 426–434, Mar. 2010, doi: 10.1364/JOSAA.27.000426.

[6] C. Akcay, P. Parrein P, and J. P. Rolland, "Estimation of longitudinal resolution in optical coherence imaging," *Appl. Opt.*, vol. 41, no. 25, pp. 5256–5262, Sep. 2002, doi: 10.1364/AO.41.005256.

[7] M. Tsang, R. Nair, and X. Lu, "Quantum theory of superresolution for two incoherent optical point sources," *Phys. Rev. X*, vol. 6, no. 3, Aug. 2016, Art. no. 031033, doi: 10.1103/PhysRevX.6.031033.

[8] M. Paúr *et al.*, "Tempering Rayleigh's curse with PSF shaping," *Optica*, vol. 5, no. 10, pp. 1177–1180, Sep. 2018, doi: 10.1364/OPTICA.5.001177.

[9] G. Tang, A. C. Hourd, and A. Abdolvand, "Nanosecond pulsed laser blackening of copper," *Appl. Phys. Lett.*, vol. 101, no. 23, Dec. 2012, Art. no. 231902, doi: 10.1063/1.4769215.

[10] M. Duocastella and C. B. Arnold, "Enhanced depth of field laser processing using an ultra-high-speed axial scanner," *Appl. Phys. Lett.*, vol. 102, no. 6, Feb. 2013, Art. no. 061113, doi: 10.1063/1.4791593.

[11] A. Sainte-Marie, O. Gobert, and F. Quéré, "Controlling the velocity of ultrashort light pulses in vacuum through spatio-temporal couplings," *Optica*, vol. 4, no. 10, pp. 1298–1304, Oct. 2017, doi: 10.1364/OPTICA.4.001298.

[12] R. Chen *et al.*, "High efficiency all-fiber cylindrical vector beam laser using a long-period fiber grating," *Opt. Lett.*, vol. 43, no. 4, pp. 755–758, Feb. 2018, doi: 10.1364/OL.43.000755.

[13] B. Guo *et al.*, "Ultra-long-period grating-based multi-wavelength ultrafast fiber laser," *Chin. Opt. Lett.*, vol. 19, no. 7, Jul. 2021, Art. no. 071405, doi: 10.3788/COL202119.071405.

[14] D. H. Froula *et al.*, "Spatiotemporal control of laser intensity," *Nature Photon.*, vol. 12, no. 5, pp. 262–265, May 2018, doi: 10.1038/s41566-018-0121-8.

[15] G. Xu, H. Zhu, T. Wang, and L. Qian, "Large high-order nonlinear phase shifts produced by $\chi^{(2)}$ cascaded processes," *Opt. Commun.*, vol. 207, no. 1–6, pp. 347–351, Jun. 2002, doi: 10.1016/S0030-4018(02)01484-0.

[16] Y. Wang *et al.*, "Spatiotemporal couplings through a nonlinear phase in broadband optical parametric amplification," *Opt. Lett.*, vol. 46, no. 22, pp. 5743–5746, Nov. 2021, doi: 10.1364/OL.440145.

[17] A. Giree *et al.*, "Numerical study of spatiotemporal distortions in non-collinear optical parametric chirped-pulse amplifiers," *Opt. Exp.*, vol. 25, no. 4, pp. 3104–3121, Feb. 2017, doi: 10.1364/OE.25.003104.

[18] J. Bromage, C. Dorrer, and J. D. Zuegel, "Angular-dispersion-induced spatiotemporal aberrations in noncollinear optical parametric amplifiers," *Opt. Lett.*, vol. 35, no. 13, pp. 2251–2253, Jul. 2010, doi: 10.1364/OL.35.002251.

[19] T. Eichner *et al.*, "Spatio-spectral couplings in saturated collinear OPCPA," *Opt. Exp.*, vol. 30, no. 3, pp. 3404–3415, Jan. 2022, doi: 10.1364/OE.448551.

[20] A. Jeandet *et al.*, "Survey of spatio-temporal couplings throughout high-power ultrashort lasers," *Opt. Exp.*, vol. 30, no. 3, pp. 3262–3288, Jan. 2022, doi: 10.1364/OE.444564.

[21] I. N. Ross, P. Matousek, G. H. C. New, and K. Osvay, "Analysis and optimization of optical parametric chirped pulse amplification," *J. Opt. Soc. Amer. B*, vol. 19, no. 12, pp. 2945–2956, Dec. 2002, doi: 10.1364/JOSAB.19.002945.

[22] J. Moses, C. Manzoni, S. Huang, G. Cerullo, and F. X. Kärtner, "Temporal optimization of ultrabroadband high-energy OPCPA," *Opt. Exp.*, vol. 17, no. 7, pp. 5540–5555, Mar. 2009, doi: 10.1364/OE.17.005540.

[23] J. Rosen, N. Siegel, and G. Brooker, "Theoretical and experimental demonstration of resolution beyond the Rayleigh limit by FINCH fluorescence microscopic imaging," *Opt. Exp.*, vol. 19, no. 27, pp. 26249–26268, Dec. 2011, doi: 10.1364/OE.19.026249.

[24] S. C. Wilks, J. M. Dawson, and W. B. Mori, "Frequency up-conversion of electromagnetic radiation with use of an overdense plasma," *Phys. Rev. Lett.*, vol. 61, no. 3, pp. 337–340, Jul. 1988, doi: 10.1103/PhysRevLett.61.337.

[25] J. Ren *et al.*, "A new method for generating ultraintense and ultrashort laser pulses," *Nature Phys.*, vol. 3, no. 10, pp. 732–736, Sep. 2007, doi: 10.1038/nphys717.

[26] S. M. Hooker, "Developments in laser-driven plasma accelerators," *Nature Photon.*, vol. 7, no. 10, pp. 775–782, Sep. 2013, doi: 10.1038/nphoton.2013.234.

[27] A. Butler *et al.*, "Demonstration of a collisionally excited optical-field-ionization XUV laser driven in a plasma waveguide," *Phys. Rev. Lett.*, vol. 91, no. 20, Nov. 2003, Art. no. 205001, doi: 10.1103/PhysRevLett.91.205001.

[28] N. D. Powers *et al.*, "Quasi-monoenergetic and tunable X-rays from a laser-driven Compton light source," *Nature Photon.*, vol. 8, no. 1, pp. 28–31, Nov. 2014, doi: 10.1038/nphoton.2013.314.